Impacts of Focused Ion Beam Processing on the Fabrication of Nanoscale Functionalized Probes

Xiang Wang[†], Sandra D. Taylor[†], Michel Sassi[†], Sichuang Xue[†], Zhenzhong Yang[†], Jia Liu[§], Lili Liu[§], Xiaoxu Li[†], Yingge Du[†], Kevin M. Rosso[†,*], and Xin Zhang[†,*]

[†] Physical & Computational Science Directorate, Pacific Northwest National Laboratory, Richland, Washington 99354, United State

[§] Energy and Environment Directorate, Pacific Northwest National Laboratory, Richland, Washington 99354, United State

Corresponding authors: Xin Zhang (xin.zhang@pnnl.gov) and Kevin M. Rosso (kevin.rosso@pnnl.gov).

ABSTRACT

Herein, we examine the impact of Ga^+ ion kinetic energy and the target material type on the extent of ion implantation and structural damage in atomic force microscopy probes made of Al_2O_3 and ZnO manufactured by focused ion beam (FIB) using scanning transmission electron microscopy and energy-dispersive X-ray mapping. Penetration of Ga into the Al_2O_3 lattice induced structural distortions and amorphization. For ZnO probes, Ga is uniformly dispersed across the surface, resulting in the formation of distinct clusters. Atom probe tomography further validates the Ga distributions in Al_2O_3 and ZnO nanoprobes. Complementary Monte Carlo simulations with the transport of ions in the matter program indicated that the introduction of Ga^+ prompts the generation of cation and anion vacancies, an occurrence more pronounced in Al_2O_3 compared to

22 ZnO. This study not only enriches the knowledge of ion-matter interactions, but also serves as a
23 practical guide for the fabrication of nanoscale functionalized AFM probes.

24 **KEYWORDS:** *functionalized AFM probes, FIB milling, Ga^+ implantation, structural damage,*
25 *Al_2O_3, ZnO.*

26 INTRODUCTION

27 A fundamental understanding of crystal growth pathways, surface friction, and material
28 rheology can be gained by directly probing interaction forces between particles. For example,
29 particle-based crystallization pathways, such as oriented attachment (OA), are profoundly
30 influenced by the interactions between nanocrystals[1-4]. Measuring interaction forces between
31 crystals is crucial, and atomic force microscopy (AFM) using customized nanoprobes is a
32 prevalent technique for this purpose[5, 6]. However, a key challenge lies in preparing probes suitable
33 for direct and specific force measurements among diverse crystal types. The ideal preparation of
34 the AFM probe requires a smooth surface[7, 8] and a desired crystallographic orientation to constrain
35 the atomic structure at the end of the tip[9, 10]. Focused ion beam (FIB) milling techniques have been
36 extensively employed in the fabrication of advanced micro/nanodevices [11, 12] and preparing
37 samples in materials science [13, 14]. Through the strong collision of incoming ions with the target
38 material, FIB is used to isolate and extract sections from select locations at the micrometer scale.
39 These sections are subsquently further transformed by FIB into suitable architectures and
40 thicknesses at the nanometer scale, such as those required for atom probe tomography (APT)[15, 16]
41 and transmission electron microscopy (TEM)[17] samples. This technique allows precise targeting
42 of specific sources of material sites and is applicable to the study of various materials, from
43 nanoparticles to natural bulk minerals[14].

44 Our group has recently developed innovative FIB milling-based protocols for preparing
45 oriented nanocrystal AFM tips[18], enabling precise measurements between mutually oriented
46 nanocrystal-nanocrystal interaction forces using either an *in situ* TEM-AFM technique or AFM-
47 based dynamic force spectroscopy[19-21]. These methods have been applied to directly determine van
48 der Waals attraction between rutile nanocrystals (TiO_2) nanocrystals[22] and interaction forces
49 between zinc oxide (ZnO) crystals during their oriented attachment growth[23]. In particular, this
50 approach affords the flexibility to adjust the orientation relation between two crystals to measure
51 how their interaction forces change as a function of the relative orientation of their crystal lattices[22,
52 23].

53 It is well known that energetic ions used for FIB milling (eg, Ga^+) can interact with the
54 target material, making it important to consider how alterations at the surface of the nanoprobe,
55 including ion implantation,[24, 25] defect formation,[26] structural damage,[27-29] or phase
56 transformation,[13, 27, 28, 30-32] can affect its functionality and properties. For example, the introduction
57 of a surface-defected layer in a single-crystal ZnO has been demonstrated to enhance its electrical
58 conductivity[33]. The extent of FIB-induced damage is dependent on critical processing parameters,
59 including the ion energy[34, 35] and ion types[36-39]. In particular, minimizing ion energy has proven to
60 be effective in reducing the thickness of a FIB-induced amorphous layer in silicon[34]. Additionally,
61 Eder *et al.*[39] demonstrated that xenon ions (Xe^+) exhibit the most shallow implantation depth in
62 FIB-prepared APT tungsten (W) tips compared to argon (Ar^+), nitrogen (N^+) and oxygen (O^+) ion
63 sources. Furthermore, it is important to acknowledge that distinct materials manifest diverse
64 responses to ion bombardment even when subjected to identical processing parameters[40, 41]. These
65 observations underscore the necessity of a comprehensive exploration into ion-beam-induced
66 damage in nanoscale functionalized AFM tips during FIB milling. Such an inquiry is essential to

67 provide explicit guidelines aimed at minimizing surface damage and meticulously selecting
68 processing parameters to ensure the fabrication of high-quality AFM probes.

69 In this study, we investigate the FIB-induced structural evolution and potential Ga^+
70 contamination in functionalized AFM nanoprobes made from corundum (Al_2O_3) and ZnO, using
71 high-resolution scanning transmission electron microscopy (STEM), energy-dispersive X-ray
72 (EDX) mapping, and atom probe tomography (APT). Al_2O_3 and ZnO were specifically selected
73 due to their distinct roles in crystal growth and surface interaction studies. ZnO, a well-studied
74 material in oriented attachment processes, serves as an excellent model for exploring particle-
75 based crystallization mechanisms, while Al_2O_3 provides an ideal platform for investigating friction
76 and wear properties at the nanoscale due to its robust hardness and stability.[42-46] Additionally, these
77 two materials exhibit a significant contrast in hardness, which in turn influences their response to
78 FIB Ga^+ ion sources. Al_2O_3, with its high hardness, may exhibit a different resistance to
79 implantation of Ga^+ ions compared to softer ZnO, which affects the extent of surface
80 amorphization and penetration of Ga^+ during FIB milling. Moreover, understanding the impact of
81 FIB processing on these materials is essential, as it directly influences their performance and
82 reliability in electronic applications. Here, two distinct functionalized AFM probes were fabricated
83 from base materials Al_2O_3 and ZnO using a specialized FIB milling protocol developed within our
84 research group[18]. A particular focus was placed on discerning the ramifications of varying ion
85 energy levels, ranging from 5 to 1 kV, when applied to the fabrication of Al_2O_3 probes. Furthermore,
86 transport of ions in matter (TRIM) simulations are performed, providing information on the
87 disparities of Ga^+-induced damage observed between Al_2O_3 and ZnO nanoprobes prepared by FIB
88 milling. By combining advanced characterization techniques with simulations, this work advances
89 understanding of the intricate interplay between ion-solid interactions and materials response as

90 well as provides tangible guidelines for the fabrication of nanoscale functionalized AFM probes
91 and associated semiconductor devices.

92 **EXPERIMENTAL SECTION**

93 **FIB process and sample preparation** The Al_2O_3 (sapphire) and ZnO substrates used in this study
94 were obtained from MTI Corporation (Richmond, California). The Al_2O_3 substrates is a c-plane
95 (0001) single-crystal wafter with a size of 5 × 5 × 0.5 mm, while the ZnO substrate is a (0001)
96 orientated single-crystal wafer with the same dimensions. Both substrates are non-conductive and
97 have well-defined crystallographic orientations. Fabrication of Al_2O_3 and ZnO probes was carried
98 out in FIB-SEM (Helios NanoLab 600i, FEI, Hillsboro, OR). More details about our FIB process
99 can be found in our previous paper published in Nature Protocols.[18] No uncommon hazards are
100 noted.

101 **S/TEM characterization** STEM-HAADF was performed at a Titan 80-300 monochromated
102 scanning TEM (Thermo Fisher Scientific) under the operating voltage 300 kV, which was equipped
103 with a probe aberration corrector. A silicon solid-state detector (AZTEC X-Max detector, Oxford)
104 fitting with the microscopy was used to capture EDX maps.

105 **Atom probe tomography** To capture the Ga at the Al_2O_3 surface with APT, the tips were coated
106 with Ti using the ion-beam sputter deposition (IBSD; South Bay Technologies) system; Ti was
107 chosen as it was thought to potentially adhere well to the Al_2O_3 due to its ability to adopt the
108 corundum structure. It also does not present considerable isobaric/polyatomic interferences in the
109 mass spectra with the major ions of interest (e.g., Al and Ga) compared to more common coating
110 materials (e.g. Cr coating present potential interferences between $^{54}Cr^{++}$ and $^{27}Al^{+}$). Al is a minor
111 component present in the coating from the IBSD target holder. To capture the Ga at the ZnO surface

112 the tips were coated with Ni using the IBSD system. Ni was chosen as it was thought to be able to
113 adhere to the ZnO surface as NiO. A CAMECA Local Electrode Atom Probe 4000 X-HR housed
114 in the Environmental Molecular Sciences Laboratory (EMSL) at Pacific Northwest National
115 Laboratory (PNNL) was used for APT analysis. Tips were run at a base temperature of 40 K, a
116 laser pulse repetition rate of 250 kHz, laser energy of 60 – 100 pJ, and a detection rate of 0.002 –
117 0.003 ions per pulse (maintained by varying the applied specimen voltage).

118 3D chemical reconstructions were achieved using the Integrated Visualization and Analysis
119 Software (IVAS 3.8.5) developed by CAMECA, specifying a nominal atomic density consistent
120 with that of Al_2O_3 (i.e., 0.00842 nm^{-3}) and a nominal atomic density consistent with that of ZnO
121 (i.e., 0.0124 nm^{-3}). Two APT specimens were measured, one specimen is presented here as a
122 representative. The distribution of Ga relative to the Al_2O_3 substrate and the Ti-coating was
123 visualized using dominant ionic species within the mass spectra. In particular, Ga was visualized
124 using $^{69}Ga^{1+}$ at 69Da (~1.3 ion%). The metallic Ti-coating was visualized with $^{48}Ti^{2+}$ at 24Da (~25
125 ion%). Due to the presence of Al in the Ti-coating, largely as simple Al ionic species (e.g., Al^{1+} at
126 27Da), Al_2O_3 was best visualized using the $^{27}Al^{16}O^{1+}$ species at 43Da (2.3 ion%). For simplicity,
127 these species will be referred to as Ti, Al, and Ga thereafter. Interpreting the Ga distribution relative
128 to the ZnO substrate and the Ni-coating required considerations of isobaric/polyatomic
129 interferences in the mass spectra. For instance, the ions at 69Da may be convoluted where $^{69}Ga^{1+}$
130 is dominant though the signal may be affected by contributions from $^{68}Zn^{1}H^{1+}$ potentially present.
131 Additionally, isobaric interferences exist between ^{64}Ni and ^{64}Zn species and thus can yield Ni-ZnO
132 interfaces that appear to be intermixed. With these considerations in mind ionic species, the Ga
133 distribution was best visualized using $^{69}Ga^{2+}$ at 34.5Da (~0.1 ion%), where ZnH species were not
134 readily observed. The Ni-coating was visualized using $^{58}Ni^{1+}$ at 58Da (~38 ion%) while ZnO was

135 best visualized using $^{66}Zn^{1+}$ at 66Da (~2.5 ion%, where interferences from ZnH or Ni species
136 would not be present). For simplicity, these species will be referred to as Ni, Zn, and Ga thereafter.

137 **TRIM simulation** TRIM simulations used the 2013 version of the SRIM/TRIM programs.[47] The
138 calculations used a total of 100,000 Ga ion at a kinetic energy of 1 kV and a 0° incidence angle on
139 a single layer of either Al_2O_3 or ZnO materials. The density of the Al_2O_3 and ZnO layer was set to
140 3.95 g/cm^3 and 5.61 g/cm^3 respectively. The thresdhold displacement energies for Al and O in
141 Al_2O_3 were 20 eV and 50 eV respectively,[48] while for Zn and O in ZnO, the threshold energies
142 were 50 eV and 55 eV respectively.[48]

143 **RESULTS AND DISCUSSION**

144 **Effect of ion kinetic energy.** To examine the influence of ion energy on surface damage,
145 FIB made three Al_2O_3 probes using variable accelerating voltages. The comprehensive fabrication
146 procedure is described in the *EXPERIMENTAL SECTION*. The Ga^+ ion beam was perpendicular
147 to the top surface of the nanoprobe, and the probe length is oriented along the direction [0001].
148 **Figure 1** illustrates an Al_2O_3 nanoprobe sharpened at 5 kV. The probe exhibits multiple
149 steps/shoulders due to stepwise sharpening, decreasing the inner diameter at each step of annular
150 milling (**Fig. 1a**). The diameter at the probe apex is ~ 50 nm, enabling high-resolution high-angle
151 annular dark-field scanning TEM (HAADF-STEM) imaging[49]. **Figs. 1b-c** highlight regions
152 damaged by Ga during FIB milling. To start, the shanks show mild doping of heavier Ga atoms
153 into the Al_2O_3 structure (Fig.1 b and d), as revealed by the contrast z in the HAADF-STEM images.
154 Implantation of ions leads to the formation of Ga-enriched domains as well as an amorphized layer
155 at the surface ~7 nm thickness surface. EDX mapping (Figs. 1 e-h) confirmed the enrichment of
156 Ga on the apex and shoulders of the nanoprobe rather than its lateral surface.

157

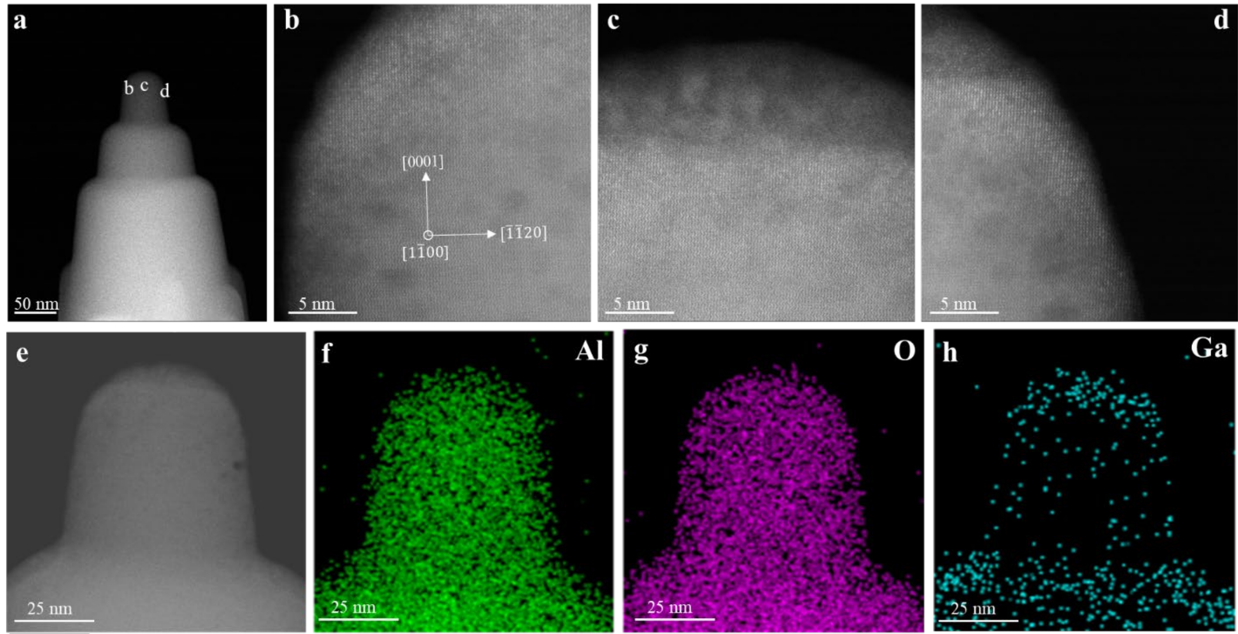

158 **Figure 1.** Al_2O_3 probe sharpened at 5kV. (a) HAADF-STEM image of Al_2O_3 probe. (b-d) Enlarged
159 HAADF-STEM images of selected areas marked in a. (e) STEM image of probe top for EDX
160 mapping. (f-h) EDX maps for Al_k, O_k, and Ga_k in e.

161

162 To mitigate surface damage, the ion acceleration voltage for the second fabricated
163 nanoprobe was reduced to 2 kV during the final milling step (**Figure 2**), resulting in a ~16 nm
164 diameter at the apex. Similarly to the 5kV case (**Figure 1**), multiple steps are formed after milling,
165 although they show smoother transitions (**Fig. 2a**). High resolution HAADF imaging reveals a
166 damaged layer of ~3 nm thickness, with some clusters at the probe apex (**Fig. 2c**). The observed
167 lattice structure in the damaged layer indicates that some crystalline structure is retained, although
168 it is different from the pristine Al_2O_3 (**Fig. 2c**). In contrast to the significant damage at the apex,
169 the probe shanks retained the lattice structure, suggesting they underwent Ga doping instead of the
170 structure degradation (**Figs. 2 b** and **d**). This observation is consistent with that for the 5kV probe
171 (**Fig. 1**). The dark areas in **Figs. 2 b-d** result from material redeposition during milling. Subsequent
172 EDX maps confirmed the heterogeneous distribution of Ga on the probe surface, with Ga

173 concentrated around steps (**Figs. 2e-h**) though less concentrated than that observed at 5kV (**Fig.**
174 **2h**). These findings indicate that a lower accelerating voltage effectively reduces damage by Ga^+-
175 ion bombardment.

176
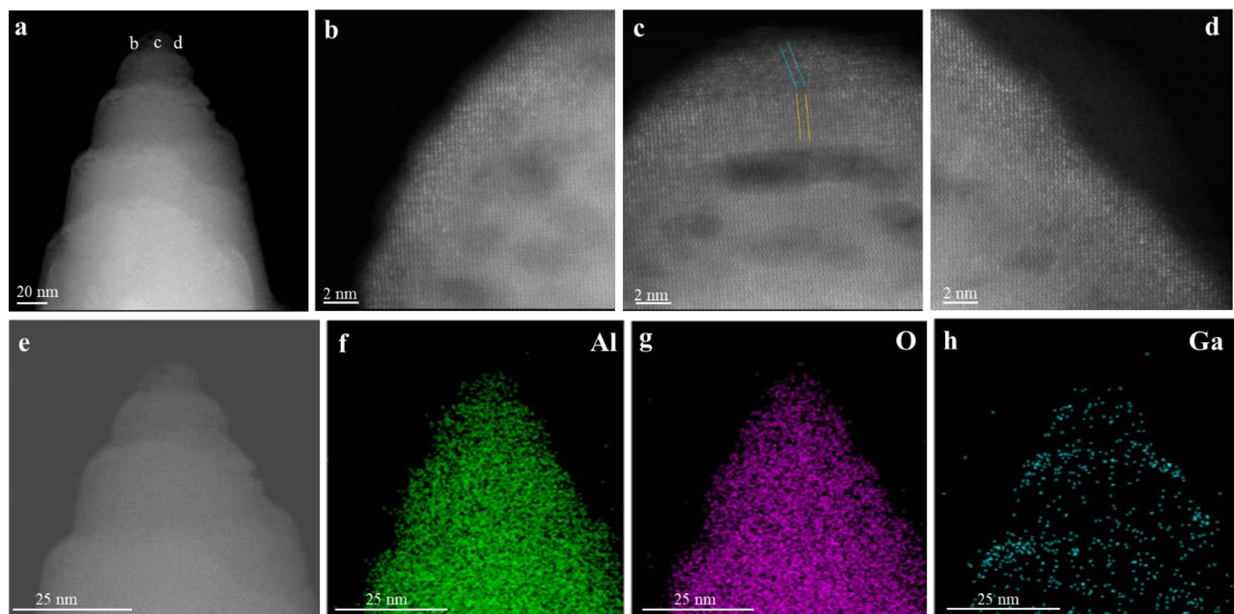

177
178 **Figure 2.** Al_2O_3 probe sharpened at 2 kV. (a) HAADF-STEM image of Al_2O_3 probe. (b-d)
179 Enlarged HAADF-STEM images of selected areas marked in a. Lattice was marked by color lines.
180 (e) STEM image of probe top for EDX mapping. (f-h) EDX maps for Al_K, O_K, and Ga_K in e.
181

182 Further reducing the acceleration voltage to 1 kV yields a sharper Al_2O_3 probe, as shown
183 in **Figure 3**; that is, the diameter of the probe apex is ~ 16 nm and the shank shows a smoother
184 profile with shallow steps (**Fig. 3a**). High-magnification HAADF-STEM images of the apex show
185 that the surface retains the original structure with a lower amount of Ga doping (Figs. 1 b and d),
186 thus indicating less damage at this condition. Damage and enrichment of Ga are concentrated at
187 the probe apex, within a thin amorphous layer <2 nm thick (**Fig. 3c**). The EDS profiles, normalized
188 by the counts of Al, show that the Ga counts across the probes decrease as the Ga^+ ion voltage
189 decreases from 5 kV to 2 kV and then to 1 kV, as illustrated in **Fig. S1**. The corresponding atomic

190 concentrations of Ga are 1.2%, <0.1%, and <0.1%, respectively, indicating that further lower Ga^+

191 ion voltage reduces Ga contamination. Notably, there is a relatively even distribution of Ga over

192 the probe surface, slightly more concentrated at the apex and the shoulders between surface steps.

193

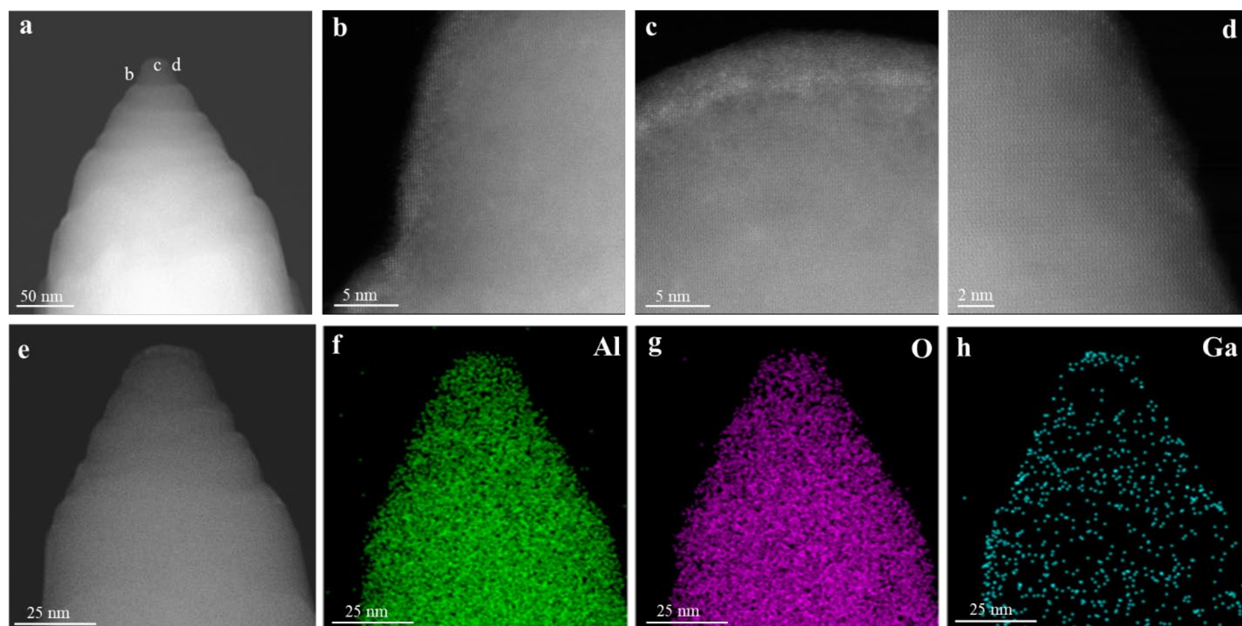

194 **Figure 3.** Al_2O_3 probe sharpened at accelerating voltage 1kV. (a) HAADF-STEM image of Al_2O_3

195 probe. (b-d) Enlarged HAADF-STEM images of selected areas marked in a. (e) STEM image of

196 probe top for EDX mapping. (f-h) EDX maps for Al_k, O_k, and Ga_k in e.

197

198 APT analysis of an Al_2O_3 nanoprobe sharpened at 1 kV further reveals site-specific Ga

199 distributions in 3D with nanometer-scale resolution. As described in the *EXPERIMENTAL*

200 *SECTION*, the nanoprobe was conformally coated with Ti to capture the surface region. The atomic

201 map reconstruction captures the general morphology of the nanoprobe, showing a nanoscale step

202 and a slight shoulder along the probe's shank (**Fig. 4, Video S1**), consistent with TEM observations.

203 Minor spatial distortions may occur at the Ti-Al_2O_3 interface due to field evaporation effects [50, 51].

204 Nonetheless, the Ga is shown to be nonrandomly distributed on the Al_2O_3 surface, as it is highly

205 localized on the step shoulders with less along the shank, as shown by both atomic maps and a 2D

206 concentration plot of Ga (**Figs. 4 b** and **c**). It is reasonable that the shoulders exhibit more Ga than
207 the shanks along the Al_2O_3 nanoprobe, as these areas are more resistant to milling and thus
208 accumulate more Ga damage.

209 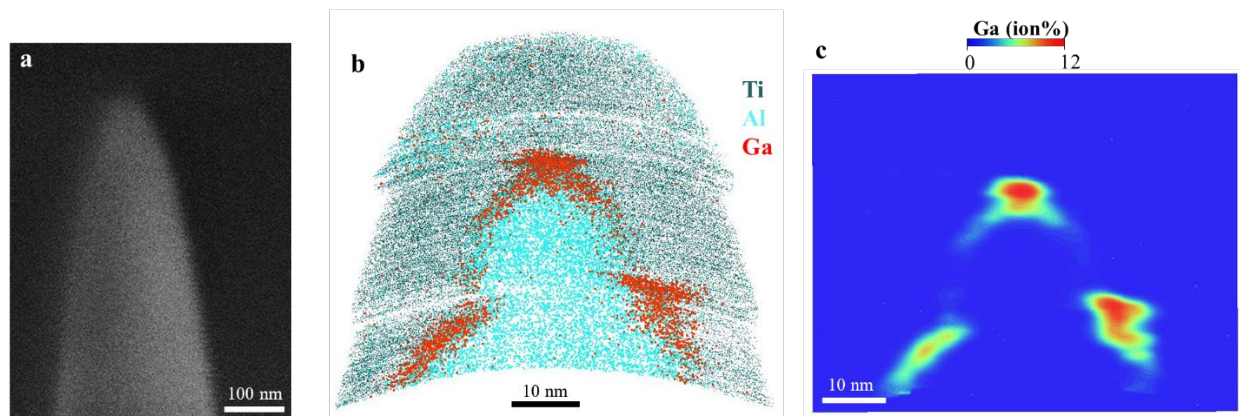

210 **Figure 4.** Atom probe tomography of FIB-fabricated Al_2O_3 probe sharpened at 1kV. (a) SEM
211 image. (b) Corresponding atomic map showing the distribution of Ga, Ti, and Al within a 10nm
212 slice of the reconstructed tip. Note the Ga ions are enlarged to highlight their localization on the
213 shoulders of Al_2O_3. (c) 2D contour plot showing the concentration of Ga within the tip.
214

215 The sputtering threshold energy for alumina is approximately 20 eV[52], which is a critical
216 value for initiating the sputtering process. The ion beam energies used in this context are
217 sufficiently high to exceed this threshold, thus enabling the sputtering of alumina. The variation in
218 kinetic energy imparted by three distinct accelerating voltages results in different implantation
219 depths and varying thicknesses of the damage layer within the alumina substrate, as shown in Table
220 1. The sputtering rate (R) has been reported to be directly proportional to both the sputtering yield
221 (Y) and the beam current (I)[53]. The sputtering yield roughly scales with the ion beam energy,
222 which depends on the accelerating voltage, based on Yamamura and Tawara formula[54, 55]. With
223 increasing accelerating voltages, there is a corresponding increase in both the sputtering yield and
224 the rate. This enhanced sputtering activity is evidenced by the formation of distinct steps or

225 shoulders on the alumina probes. Moreover, the elevated sputtering yield associated with higher
226 incident voltages also promotes the creation of defects deeper within the alumina substrate.
227 Furthermore, an increase in accelerating voltage results in a deeper penetration of Ga^+ ions into
228 the target material[47]. This deeper penetration contributes to changes in the physical structure of
229 alumina, which could affect its mechanical and electrical properties[26]. Specifically, when Al_2O_3
230 used as a dielectric layer in semiconductors, Ga contamination and amorphization in Al_2O_3 may
231 degrade its insulating properties, increasing leakage currents[48] . As a substrate for epitaxial
232 nanostructures support that require precise control over material characteristics at the microscopic
233 level, induced defects and chemical changes can affect adhesion and crystallinity[44]. Furthermore,
234 in the tribological applications, such as in wear-resistant coatings and micro-electromechanical
235 systems (MEMS), may also be affected due to the degradation of its mechanical integrity.

236

237 **Table 1.** Milling parameters for three Al_2O_3 probes and corresponding impact.

Accelerating voltage (kV)	Current (pA)	Diameter of the probe top (nm)	Ga Ion implantation depth (nm)	The thickness of the amorphous layer (nm)
5	4.4 and 1.6	~50	~7.5	~7
2	3.2 and 1.3	~16	~3.2	~3
1	1-2	~16	~3.8	< 2

238

239

240 **Effect of the target materials.** ZnO is a widely studied oxide characterized by a hexagonal
241 wurtzite crystal structure, which distinguishes it as a semiconductor,[56] in contrast to Al_2O_3. To
242 explore the effect of target materials on FIB-induced damage, a ZnO nanoprobe was fabricated

243 with a Ga ion beam with an acceleration voltage of 1 kV, as illustrated in **Figure 5**. To mitigate the
244 severe damage induced by high processing voltages, a voltage of only 1 kV was selected to
245 investigate the effects of the target materials. The nanoprobe length was oriented along [001].
246 Differently from previously fabricated Al_2O_3 probes, the ZnO probe exhibits a more slender profile
247 (**Fig. 5a**), suggesting a greater potential for sharpness under comparable processing parameters
248 compared to Al_2O_3. The diameter of the probe apex reaches ~ 10 nm, significantly less than those
249 of the Al_2O_3 probes. Interestingly, in contrast to surface amorphization observed in Al_2O_3 probes,
250 the surface of the ZnO probe maintains its crystalline structure after FIB milling, evidenced by the
251 lattice structure in the high-resolution HAADF-STEM image (**Fig. 5b**). It should be noted that
252 numerous clusters, smaller than 1 nm, are present on the probe surface, attributed to the adsorption
253 of Ga^+ ions. The corresponding EDX maps in **Figs. 5 d-f** reveal a uniform Ga^+ distribution on the
254 surface, rather than the enrichment within the probe. Additionally, the signals of Zn and Ga show
255 some overlap, suggesting a combination of Zn and Ga to form clusters. For APT analyses, a
256 nanoprobe was conformally coated with Ni to probe the ZnO surface. The APT measurement in
257 **Figure 6** corroborates the presence of Ga-Zn clusters, showing a homogeneous Ga distribution
258 across the ZnO surface (**Figs. 6 b, c**, **Video S2**). These findings suggest that Ga ions combine with
259 Zn atoms and accumulate on the surface rather than penetrate the ZnO lattice and subsequently
260 alter the structure of the target material, contrary to what was observed with the Al_2O_3 probes.

261

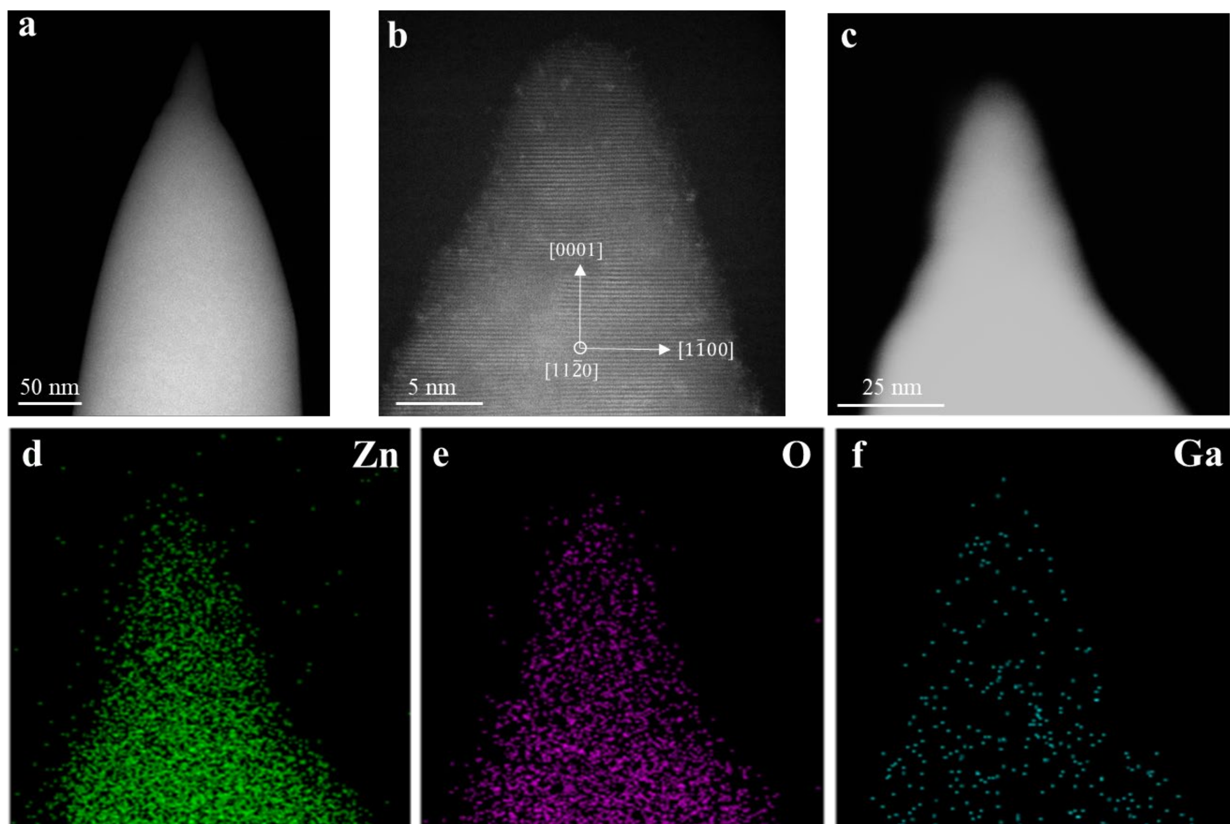

262 **Figure 5.** ZnO probe sharpened at accelerating voltage 1kV. (a) HADDF-STEM image of ZnO
263 probe. (b) High-resolution HAADF-STEM image of probe top. (c) STEM image of probe top for
264 EDX mapping. (d-f) EDX maps for Zn_K, O_K, and Ga_K in c.

265
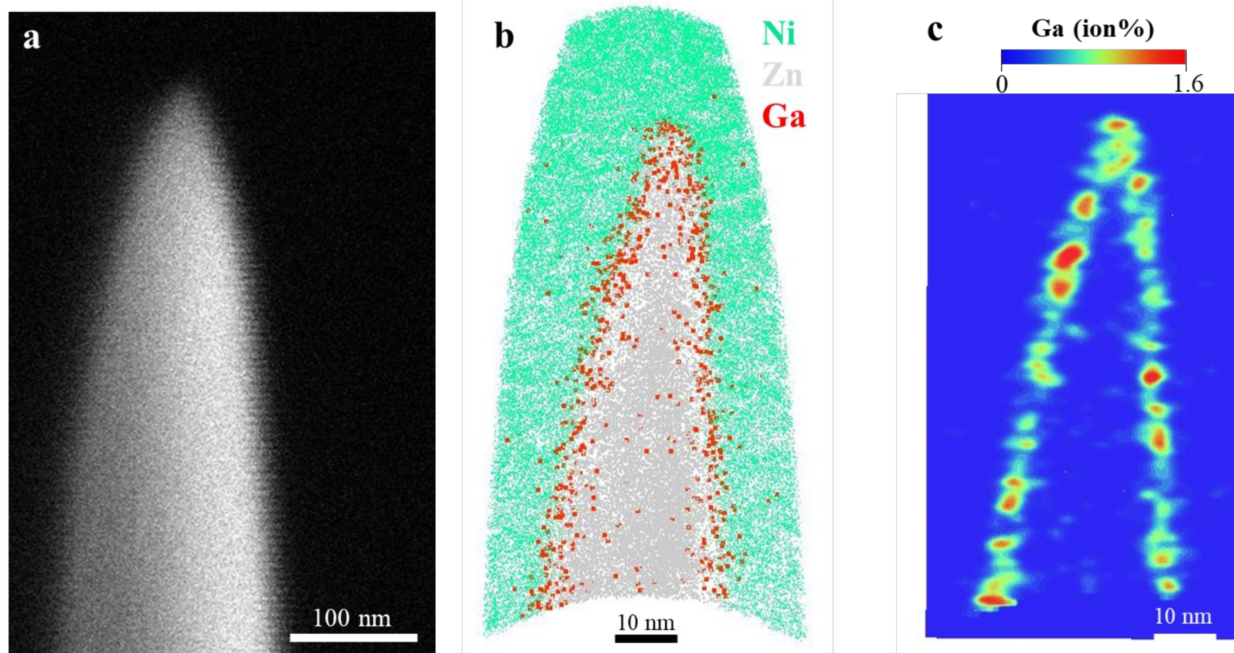

266 **Figure 6.** Atom probe tomography of ZnO probe sharpened at accelerating voltage 1kV. (a) SEM
267 image. (b) Corresponding atomic map showing the distribution of Ga, Ni, and Zn within a 10nm
268 slice of the reconstructed tip. Note the Ga ions are enlarged to highlight their localization on the
269 shoulders of ZnO. (c) 2D contour plot showing the concentration of Ga within the tip.
270

271 To elucidate the underlying mechanism inducing different damage effects in these two target
272 materials, a Monte Carlo simulation for the transport of ions in matter (TRIM)[57] was carried out
273 to meticulously track the trajectory and impact of the ions in the Al_2O_3 and ZnO probes milled
274 with FIB. As illustrated in **Figure 7**, a comparative study of the Al_2O_3 and ZnO probes reveals a
275 pronounced difference in how the cation vacancies are distributed with depth. In particular, the
276 Al_2O_3 probe exhibits a higher concentration of cation vacancies and an extended zone of influence
277 than its ZnO counterpart under an identical accelerating voltage during the FIB process. This
278 variation in depth-dependent behavior is partly due to the dissimilar crystalline structures of the
279 two materials. Specifically, the spacings of the (0001) planes are 2.17 Å for Al_2O_3 and 2.61 Å for

280 ZnO, which influences how the lattice accommodates defects. Furthermore, the trend observed in
281 cation vacancies is mirrored in the formation of anion vacancies, with oxygen vacancies being
282 more prevalent in Al_2O_3 than in ZnO. This higher susceptibility of Al_2O_3 to vacancy formation
283 suggests that its crystal structure is more amenable to transition to an amorphous state, as
284 evidenced in **Figures 1- 3**. Thus, the introduction of vacancy defects may facilitate Ga doping
285 within the crystal lattice.

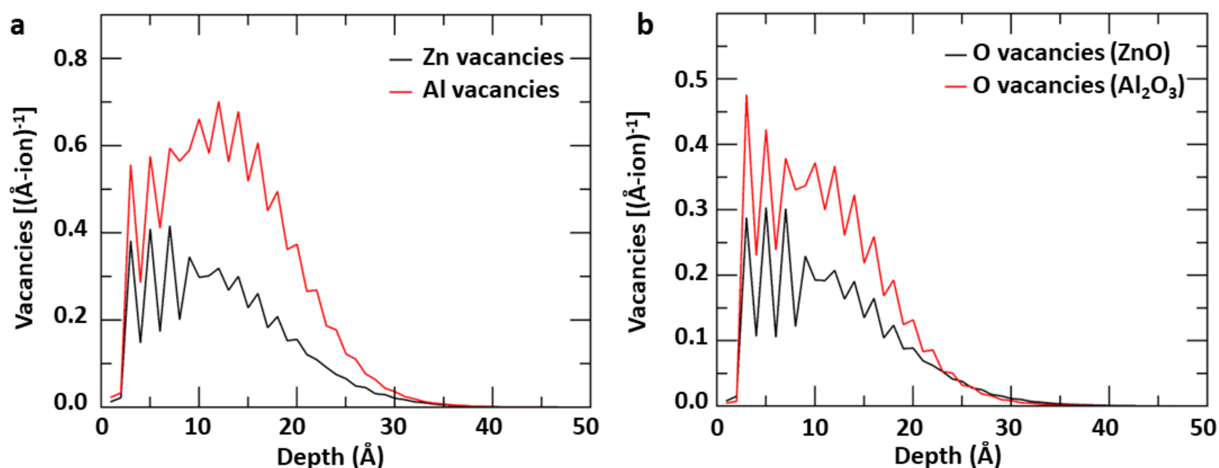

286

287 **Figure 7.** TRIM Simulations of damage profiles as a function of depth in Al_2O_3 and ZnO probes
288 sharpened at accelerating voltage 1 kV. (a) Cation vacancy profile. (b) Anion vacancy profile.
289

290 The mechanisms driving vacancy generation during FIB-milling are complex and involve
291 intricate interactions between high-energy ions and the crystal lattice. Al_2O_3, with its corundum
292 structure, and ZnO, with its wurtzite structure, respond differently to ion bombardment due to their
293 unique lattice configurations. The likelihood of atom displacement—and thus vacancy
294 production—is largely determined by the displacement energy (E_d), which is the energy threshold
295 required to eject atoms from their lattice sites [52, 58]. Referring to threshold displacement energies
296 cited in ref.[52], E_d^{Al} and E_d^{O} are ~ 20 and 50 eV respectively in Al_2O_3 while E_d^{Zn} and E_d^{O} are ~ 50

297 and 55 eV respectively in ZnO. These values suggest that under similar FIB-milling conditions,
298 cation vacancies are more readily in Al_2O_3 than in ZnO due to the lower threshold energy for
299 aluminum. Consequently, this disparity leads to a more pronounced channeling effect for Ga^+
300 implantation in Al_2O_3, resulting in a thicker layer affected by the FIB process.

301 The presence of nanoclusters at the tip apex, regardless of their composition (Ga, Zn, or
302 other elements), can significantly influence the performance of AFM probes in force measurement
303 applications. These clusters may alter the tip geometry, increasing surface roughness and affecting
304 contact mechanics, which could introduce inconsistencies in force measurements. Additionally, if
305 the clusters possess different mechanical properties than the underlying material, they may deform
306 or detach under applied forces, impacting measurement reliability. The chemical composition of
307 these clusters also plays a crucial role; for conductive clusters (e.g., metallic Zn or Ga-Zn cluster),
308 they could modify electrostatic interactions, thereby affecting measurements in force spectroscopy.
309 To mitigate these issues, optimization of FIB processing parameters, such as lowering Ga^+ ion
310 energy, has proven effective in reducing implantation depth and surface amorphization.
311 Furthermore, post-processing techniques such as annealing, plasma cleaning, or selective etching
312 can remove or redistribute surface clusters, improving probe performance. An alternative approach
313 involves using different FIB ion sources, such as Ar^+ and Xe^+, which might exhibit lower
314 implantation depths and could mitigate Ga contamination and clustering issues—an area we are
315 actively investigating.

316 By meticulously adjusting the milling voltage, it is possible to influence surface
317 amorphization and depth of ion implantation in Al_2O_3. Such precision enables the removal and
318 modification of materials at the nanoscale, crucial for advancing nanofabrication techniques.
319 Moreover, careful management of these processes also contributes to the miniaturization of

devices. As evidenced in **Figures 1-3** , utilizing a milling voltage as low as 1 kV, the probe size can be refined to approximately 10 nm. This level of miniaturization opens new avenues for the development of ultracompact devices. The distinct responses of Al_2O_3 and ZnO to FIB milling also present opportunities for selective material removal. This selectivity allows for precise sculpting or alteration of specific regions within these materials, making it an invaluable tool for creating complex structures or intricate patterns[59]. In addition, in the realm of biomedicine, the versatility of FIB fabrication techniques can be harnessed to construct nanoscale features in Al_2O_3 and ZnO materials[60]. These features can be integral components of innovative drug delivery systems[61], highly sensitive biosensors, or other cutting-edge medical devices that benefit from the unique properties conferred by nanoengineering.

CONCLUSIONS

In summary, combining S/TEM-EDS with APT and TRIM simulations, the impact of Ga^+ on FIB-fabricated functional probes of Al_2O_3 and ZnO was explored. The higher accelerated processing voltage during FIB caused deeper ion implantation and a thicker amorphous layer on the Al_2O_3 probe surface due to the higher kinetic energy of the ions. Furthermore, the damage was more prevalent at the nanoprobe apex and shoulders. Lowering the voltage effectively reduced damage. Compared to Al_2O_3, ZnO exhibited better resistance to Ga^+ bombardment. TRIM simulation indicated that Al_2O_3 shows a higher tendency to form anion/cation vacancies, leading to a deeper impact depth and a thicker surface amorphous layer. The underlying reason is the difference in the threshold displacement energies of atoms in two materials. In addition to providing relevant information on AFM nanoprobe fabrication for applications in the fundamental understanding of crystal growth pathways, surface friction, and material rheology, this work

342 contributes to a deeper understanding of the properties of Al_2O_3 and ZnO on the nanoscale and also
343 provides some practical guidelines for the fabrication of functional semiconductor devices.

344 SUPPORTING INFORMATION

345 The Supporting Information is available free of charge at https://pubs.acs.org/doi/.

346 • EDS profiles across the Al_2O_3 probes polished under different Ga^+ ion voltages in Figs. 1,
347 2, and 3.

348 ACKNOWLEDGMENTS

349 This material is based on work supported by the U.S. Department of Energy (DOE), Office of
350 Science, Basic Energy Sciences (BES), Chemical Sciences, Geosciences, and Biosciences
351 Division through its Geosciences Program at Pacific Northwest National Laboratory (PNNL)
352 (FWP 56674). S. Xue, L. Liu, and X. Zhang also acknowledge the funding support provided by
353 Dr. Carolyn I. Pearce through the Ion Dynamics in Radioactive Environments and Materials
354 (IDREAM) program, an Energy Frontier Research Center funded by the U.S. Department of
355 Energy, Office of Science, Basic Energy Sciences (FWP 68932). A portion of the work was carried
356 out in the Environmental and Molecular Sciences Laboratory (EMSL), a national scientific user
357 facility at PNNL sponsored by the DOE's Office of Biological and Environmental Research, under
358 user proposals 61223 (10.46936/lsr.proj.2024.61223/60012698), 51382
359 (10.46936/lser.proj.2020.51382/60000186) and 51922 (10.46936/lser.proj.2021.51922/60000373).
360 PNNL is a multi-program national laboratory operated by Battelle Memorial Institute under
361 contract no. DE-AC05-76RL01830 for the DOE.

362 COMPETING INTERESTS

363 The authors declare no competing interests.

364 **REFERENCES**

365 (1) Cölfen, H.; Mann, S. Higher-order organization by mesoscale self-assembly and transformation
366 of hybrid nanostructures. *Angewandte Chemie International Edition* **2003**, *42* (21), 2350-2365.

367 (2) Niederberger, M.; Cölfen, H. Oriented attachment and mesocrystals: non-classical
368 crystallization mechanisms based on nanoparticle assembly. *Physical chemistry chemical physics*
369 **2006**, *8* (28), 3271-3287.

370 (3) Raju, M.; Van Duin, A. C.; Fichthorn, K. A. Mechanisms of oriented attachment of TiO2
371 nanocrystals in vacuum and humid environments: reactive molecular dynamics. *Nano letters* **2014**,
372 *14* (4), 1836-1842.

373 (4) De Yoreo, J. J.; Gilbert, P. U.; Sommerdijk, N. A.; Penn, R. L.; Whitelam, S.; Joester, D.; Zhang,
374 H.; Rimer, J. D.; Navrotsky, A.; Banfield, J. F. Crystallization by particle attachment in synthetic,
375 biogenic, and geologic environments. *Science* **2015**, *349* (6247), aaa6760.

376 (5) Liang, Y.; Hilal, N.; Langston, P.; Starov, V. Interaction forces between colloidal particles in
377 liquid: Theory and experiment. *Advances in colloid and interface science* **2007**, *134*, 151-166.

378 (6) Seo, Y.; Jhe, W. Atomic force microscopy and spectroscopy. *Reports on Progress in Physics*
379 **2008**, *71* (1), 016101.

380 (7) Hirz, S.; Homola, A.; Hadziioannou, G.; Frank, C. Effect of substrate on shearing properties of
381 ultrathin polymer films. *Langmuir* **1992**, *8* (1), 328-333.

382 (8) Eastman, T.; Zhu, D.-M. Adhesion forces between surface-modified AFM tips and a mica
383 surface. *Langmuir* **1996**, *12* (11), 2859-2862.

384 (9) Finot, E.; Lesniewska, E.; Mutin, J.-C.; Goudonnet, J.-P. Investigations of surface forces
385 between gypsum microcrystals in air using atomic force microscopy. *Langmuir* **2000**, *16* (9), 4237-
386 4244.

387 (10) Struczyńska, M.; Firkowska-Boden, I.; Scheuer, K.; Jandt, K. D. Rutile facet-dependent
388 fibrinogen conformation: Why crystallographic orientation matters. *Colloids and Surfaces B:*
389 *Biointerfaces* **2022**, *215*, 112506.

390 (11) Gierak, J. Focused ion beam technology and ultimate applications. *Semiconductor science*
391 *and technology* **2009**, *24* (4), 043001.

392 (12) Langford, R. M.; Nellen, P. M.; Gierak, J.; Fu, Y. Focused ion beam micro-and
393 nanoengineering. *MRS bulletin* **2007**, *32* (5), 417-423.

394 (13) Volkert, C. A.; Minor, A. M. Focused ion beam microscopy and micromachining. *MRS*
395 *bulletin* **2007**, *32* (5), 389-399.

396 (14) Mayer, J.; Giannuzzi, L. A.; Kamino, T.; Michael, J. TEM sample preparation and FIB-
397 induced damage. *MRS bulletin* **2007**, *32* (5), 400-407.

398 (15) Babinsky, K.; De Kloe, R.; Clemens, H.; Primig, S. A novel approach for site-specific atom
399 probe specimen preparation by focused ion beam and transmission electron backscatter diffraction.
400 *Ultramicroscopy* **2014**, *144*, 9-18.

401 (16) Cerezo, A.; Clifton, P. H.; Galtrey, M. J.; Humphreys, C. J.; Kelly, T. F.; Larson, D. J.; Lozano-
402 Perez, S.; Marquis, E. A.; Oliver, R. A.; Sha, G.; Thompson, K.; Zandbergen, M.; Alvis, R. L.
403 Atom probe tomography today. *Materials Today* **2007**, *10* (12), 36-42.

404 (17) Giannuzzi, L. A.; Stevie, F. A. A review of focused ion beam milling techniques for TEM
405 specimen preparation. *Micron* **1999**, *30* (3), 197-204.

406 (18) Zhang, X.; He, Y.; Liu, J.; Bowden, M. E.; Kovarik, L.; Mao, S. X.; Wang, C.; De Yoreo, J.
407 J.; Rosso, K. M. Accessing crystal–crystal interaction forces with oriented nanocrystal atomic
408 force microscopy probes. *Nature Protocols* **2018**, *13* (9), 2005-2030.

409 (19) He, Y.; Zhong, L.; Fan, F.; Wang, C.; Zhu, T.; Mao, S. X. In situ observation of shear-driven
410 amorphization in silicon crystals. *Nat Nanotechnol* **2016**, *11* (10), 866-871.

411 (20) He, Y.; She, D.; Liu, Z.; Wang, X.; Zhong, L.; Wang, C.; Wang, G.; Mao, S. X. Atomistic
412 observation on diffusion-mediated friction between single-asperity contacts. *Nature Materials*
413 **2022,** 21, 73–180.

414 (21) Wang, X.; Liu, Z.; He, Y.; Tan, S.; Wang, G.; Mao, S. X. Atomic-scale friction between single-
415 asperity contacts unveiled through in situ transmission electron microscopy. *Nature*
416 *Nanotechnology* **2022**, 1-9.

417 (22) Zhang, X.; He, Y.; Sushko, M. L.; Liu, J.; Luo, L.; De Yoreo, J. J.; Mao, S. X.; Wang, C.;
418 Rosso, K. M. Direction-specific van der Waals attraction between rutile TiO_2 nanocrystals. *Science*
419 **2017**, *356* (6336), 434-437.

420 (23) Zhang, X.; Shen, Z.; Liu, J.; Kerisit, S.; Bowden, M.; Sushko, M.; De Yoreo, J. Direction-
421 specific interaction forces underlying zinc oxide crystal growth by oriented attachment. *Nature*
422 *communications* **2017**, *8* (1), 835.

423 (24) Spolenak, R.; Sauter, L.; Eberl, C. Reversible orientation-biased grain growth in thin metal
424 films induced by a focused ion beam. *Scripta materialia* **2005**, *53* (11), 1291-1296.

425 (25) Olliges, S.; Gruber, P.; Bardill, A.; Ehrler, D.; Carstanjen, H. D.; Spolenak, R. Converting
426 polycrystals into single crystals–selective grain growth by high-energy ion bombardment. *Acta*
427 *materialia* **2006**, *54* (20), 5393-5399.

428 (26) Kiener, D.; Motz, C.; Rester, M.; Jenko, M.; Dehm, G. FIB damage of Cu and possible
429 consequences for miniaturized mechanical tests. *Materials Science and Engineering: A* **2007**, *459*
430 (1-2), 262-272.

431 (27) Rubanov, S.; Munroe, P. FIB-induced damage in silicon. *Journal of Microscopy* **2004**, *214*
432 (3), 213-221.

433 (28) Rajsiri, S.; Kempshall, B.; Schwarz, S.; Giannuzzi, L. FIB damage in silicon: Amorphization
434 or redeposition? *Microscopy and Microanalysis* **2002**, *8* (S02), 50-51.

435 (29) Pelaz, L.; Marqués, L. A.; Barbolla, J. Ion-beam-induced amorphization and recrystallization
436 in silicon. *Journal of applied physics* **2004**, *96* (11), 5947-5976.

437 (30) Pastewka, L.; Salzer, R.; Graff, A.; Altmann, F.; Moseler, M. Surface amorphization, sputter
438 rate, and intrinsic stresses of silicon during low energy Ga^+ focused-ion beam milling. *Nuclear*
439 *Instruments and Methods in Physics Research Section B: Beam Interactions with Materials and*
440 *Atoms* **2009**, *267* (18), 3072-3075.

441 (31) Michael, J. R.; Giannuzzi, L. A.; Burke, M. G.; Zhong, X. L. Mechanism of FIB-Induced
442 Phase Transformation in Austenitic Steel. *Microscopy and Microanalysis* **2022**, *28* (1), 70-82.

443 (32) Basa, A.; Thaulow, C.; Barnoush, A. Chemically induced phase transformation in austenite
444 by focused ion beam. *Metallurgical and Materials Transactions A* **2014**, *45*, 1189-1198.

445 (33) Pea, M.; Mussi, V.; Barucca, G.; Giovine, E.; Rinaldi, A.; Araneo, R.; Notargiacomo, A.
446 Focused ion beam surface treatments of single crystal zinc oxide for device fabrication. *Materials*
447 *& Design* **2016**, *112*, 530-538.

448 (34) Giannuzzi, L. A.; Geurts, R.; Ringnalda, J. 2 keV Ga+ FIB milling for reducing amorphous
449 damage in silicon. *Microscopy and Microanalysis* **2005**, *11* (S02), 828-829.

450 (35) Thompson, K.; Gorman, B.; Larson, D.; van Leer, B.; Hong, L. Minimization of Ga induced
451 FIB damage using low energy clean-up. *Microscopy and Microanalysis* **2006**, *12* (S02), 1736-
452 1737.

453 (36) Kim, C.-S.; Ahn, S.-H.; Jang, D.-Y. Developments in micro/nanoscale fabrication by focused
454 ion beams. *Vacuum* **2012**, *86* (8), 1014-1035.

455 (37) Gierak, J.; Mazarov, P.; Bruchhaus, L.; Jede, R.; Bischoff, L. Review of
456 electrohydrodynamical ion sources and their applications to focused ion beam technology. *Journal*
457 *of Vacuum Science & Technology B* **2018**, *36* (6).

458 (38) Fang, F.; Zhang, N.; Guo, D.; Ehmann, K.; Cheung, B.; Liu, K.; Yamamura, K. Towards
459 atomic and close-to-atomic scale manufacturing. *International Journal of Extreme Manufacturing*
460 **2019**, *1* (1), 012001.

461 (39) Eder, K.; Bhatia, V.; Qu, J.; Van Leer, B.; Dutka, M.; Cairney, J. M. A multi-ion plasma FIB
462 study: Determining ion implantation depths of Xe, N, O and Ar in tungsten via atom probe
463 tomography. *Ultramicroscopy* **2021**, *228*, 113334.

464 (40) Bassim, N.; De Gregorio, B.; Kilcoyne, A.; Scott, K.; Chou, T.; Wirick, S.; Cody, G.; Stroud,
465 R. Minimizing damage during FIB sample preparation of soft materials. *Journal of Microscopy*
466 **2012**, *245* (3), 288-301.

467 (41) Prenitzer, B.; Urbanik-Shannon, C.; Giannuzzi, L.; Brown, S.; Irwin, R.; Shofner, T.; Stevie,
468 F. The correlation between ion beam/material interactions and practical FIB specimen preparation.
469 *Microscopy and Microanalysis* **2003**, *9* (3), 216-236.

470 (42) Liu, L.; Nakouzi, E.; Sushko, M. L.; Schenter, G. K.; Mundy, C. J.; Chun, J.; De Yoreo, J. J.
471 Connecting energetics to dynamics in particle growth by oriented attachment using real-time
472 observations. *Nature Communications* **2020**, *11* (1), 1045.

473 (43) Hapiuk, D.; Masenelli, B.; Masenelli-Varlot, K.; Tainoff, D.; Boisron, O.; Albin, C.; Mélinon,
474 P. Oriented Attachment of ZnO Nanocrystals. *The Journal of Physical Chemistry C* **2013**, *117* (19),
475 10220-10227.

476 (44) Fons, P.; Iwata, K.; Niki, S.; Yamada, A.; Matsubara, K. Growth of high-quality epitaxial ZnO
477 films on α-Al2O3. *Journal of Crystal Growth* **1999**, *201*, 627-632.

478 (45) Park, J. Y.; Ogletree, D. F.; Salmeron, M.; Ribeiro, R. A.; Canfield, P. C.; Jenks, C. J.; Thiel,
479 P. A. High Frictional Anisotropy of Periodic and Aperiodic Directions on a Quasicrystal Surface.
480 *Science* **2005**, *309* (5739), 1354-1356.

481 (46) Liu, L.; Sushko, M. L.; Buck, E. C.; Zhang, X.; Kovarik, L.; Shen, Z.; Tao, J.; Nakouzi, E.;
482 Liu, J.; De Yoreo, J. J. Revisiting the Growth Mechanism of Hierarchical Semiconductor
483 Nanostructures: The Role of Secondary Nucleation in Branch Formation. *The Journal of Physical*
484 *Chemistry Letters* **2019**, *10* (21), 6827-6834.

485 (47) Mikmeková, Š.; Matsuda, K.; Watanabe, K.; Ikeno, S.; Müllerová, I.; Frank, L. FIB induced
486 damage examined with the low energy SEM. *Materials Transactions* **2011**, *52* (3), 292-296.

487 (48) Liu, C.; Wang, Z.; Zhang, Y.; Lü, H. Q.; Zhang, Y. Nanolaminated HfO2/Al2O3 Dielectrics
488 for High-Performance Silicon Nanomembrane Based Field-Effect Transistors on Biodegradable
489 Substrates. *Advanced Materials Interfaces* **2022**, *9,* 32, 2201477.

490 (49) Liu, J.; Cowley, J. High-resolution scanning transmission electron microscopy.
491 *Ultramicroscopy* **1993**, *52* (3-4), 335-346.

492 (50) Müller, E. W.; Tsong, T. T. Field ion microscopy, field ionization and field evaporation.
493 *Progress in surface science* **1974**, *4*, 1-139.

494 (51) MICHAEL, K. M. *ATOM-PROBE TOMOGRAPHY: The Local Electrode Atom Probe*;
495 SPRINGER, 2016.

496 (52) Zinkle, S.; Kinoshita, C. Defect production in ceramics. *Journal of Nuclear Materials* **1997**,
497 *251*, 200-217.

498 (53) Okajima, Y. Estimation of sputtering rate by bombardment with argon gas ions. *Journal of*
499 *Applied Physics* **1980**, *51* (1), 715-717.

500 (54) Yamamura, Y.; Tawara, H. ENERGY DEPENDENCE OF ION-INDUCED SPUTTERING
501 YIELDS FROM MONATOMIC SOLIDS AT NORMAL INCIDENCE. *Atomic Data and Nuclear*
502 *Data Tables* **1996**, *62* (2), 149-253.

503 (55) Cumpson, P. J.; Portoles, J. F.; Barlow, A. J.; Sano, N. Accurate argon cluster-ion sputter yields:
504 Measured yields and effect of the sputter threshold in practical depth-profiling by x-ray
505 photoelectron spectroscopy and secondary ion mass spectrometry. *Journal of Applied Physics*
506 **2013**, *114*,124313.

507 (56) Dutta, S.; Chattopadhyay, S.; Sarkar, A.; Chakrabarti, M.; Sanyal, D.; Jana, D. Role of defects in tailoring structural, electrical and optical properties of ZnO. *Progress in Materials Science* **2009**, *54* (1), 89-136.

510 (57) Ziegler, J. F.; Ziegler, M. D.; Biersack, J. P. SRIM–The stopping and range of ions in matter (2010). *Nuclear Instruments and Methods in Physics Research Section B: Beam Interactions with Materials and Atoms* **2010**, *268* (11-12), 1818-1823.

513 (58) Williford, R. E.; Devanathan, R.; Weber, W. J. Computer simulation of displacement energies for several ceramic materials. *Nuclear Instruments and Methods in Physics Research Section B: Beam Interactions with Materials and Atoms* **1998**, *141* (1), 94-98.

516 (59) Smith, K. H.; Tejeda-Montes, E.; Poch, M.; Mata, A. Integrating top-down and self-assembly in the fabrication of peptide and protein-based biomedical materials. *Chemical Society Reviews* **2011**, *40* (9), 4563-4577.

519 (60) Popescu, M.; Ungureanu, C.; Buse, E.; Nastase, F.; Tucureanu, V.; Suchea, M.; Draga, S.; Popescu, M. Antibacterial efficiency of cellulose-based fibers covered with ZnO and Al2O3 by atomic layer deposition. *Applied Surface Science* **2019**, *481*, 1287-1298.

522 (61) Pourmadadi, M.; Farokh, A.; Rahmani, E.; Shamsabadipour, A.; Eshaghi, M. M.; Rahdar, A.; Ferreira, L. F. R. Porous alumina as potential nanostructures for drug delivery applications, synthesis and characteristics. *Journal of Drug Delivery Science and Technology* **2022**, 103877.

525

526

527 **For Table of Contents Only**

528

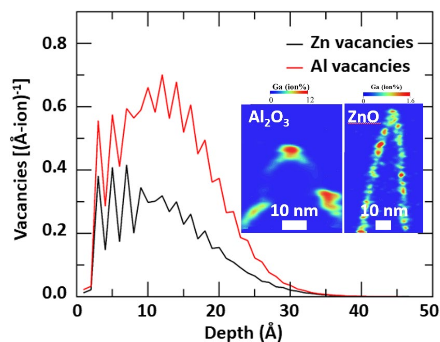

529

530 During focused ion beam processing for fabricating Al_2O_3 and ZnO nanoprobes, Ga penetration
531 into the Al_2O_3 lattice induces structural distortions and amorphization. In contrast, Ga is uniformly
532 dispersed across the ZnO surface, leading to the formation of distinct clusters.

533